www.ietdl.org

Published in IET Microwaves, Antennas & Propagation
Received on 23rd December 2013
Revised on 9th May 2014
Accepted on 21st May 2014
doi: 10.1049/iet-map.2013.0704

Special Issue on Emerging Integrated Reconfigurable Antenna Technologies

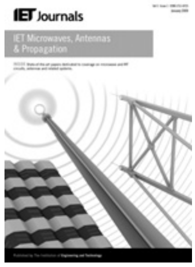

ISSN 1751-8725

Wide-angle scanning active transmit/receive reflectarray

Tobias Chaloun[1], Wolfgang Menzel[1], Filipe Tabarani[2], Tatyana Purtova[2], Hermann Schumacher[2], Mehmet Kaynak[3], Qi Luo[4], Steven Gao[4], Rado Starec[5], Volker Ziegler[6]*

[1]*Microwave Techniques, University of Ulm, PO Box, D-89081 Ulm, Germany*
[2]*Electronic Devices and Circuits, University of Ulm, PO Box, D-89081 Ulm, Germany*
[3]*IHP, Im Technologiepark 25, D-15236 Frankfurt (Oder), Germany*
[4]*School of Engineering and Digital Arts, University of Kent, Canterbury CT2 7NZ, UK*
[5]*MIPOT SpA, Via Corona, 5, I-34071 CORMONS, Italy*
[6]*EADS Innovation Works, D-81663 Munich, Germany*
**Present address: Triquint Semiconductors, Konrad-Zuse-Platz, D-81829 Munich, Germany*
E-mail: wolfgang.menzel@uni-ulm.de

Abstract: A highly integrated phased array transmit/receive architecture is presented. Multilayer microstrip antennas with a scanning potential up to 60° are combined, on a common manifold, with SiGe MMICs including four RF channels each, together with the necessary digital control circuits. Power distribution and combining are realised by the concept of a folded planar reflectarray. This study also includes the necessary solutions for multilayer interconnects and efficient heat removal from the active circuits. To prove the concept, passive arrays with different fixed beam positions have been tested successfully; followed by a first active array demonstrating excellent scanning performance up to 60° both in *E*- and *H*-plane.

1 Introduction

High data rate links for continuous mobile services have become one of the main drivers for broadband mobile Satellite Communication (SatCom) links on platforms such as airplanes, trains or ships [1, 2]. This scenario demands for the lowest possible impact of the antenna system on the mechanical structure, drag and costs. To maintain communication links while moving and to avoid bulky configurations, for example mechanical scanned antennas, an electronically steerable antenna array approach is of major importance [3–5]. Therefore this paper reports on concept, design and practical results of a transmit/receive (T/R) array for the 29–30.8 GHz frequency range. On the one hand, this work is a first study for 20/30 GHz SATCOM transceivers (with further effort necessary for the 20 GHz downlink). Alternative application in similar frequency bands such as terrestrial communications in the 28/29 GHz band or sensor applications may be also covered by this approach.

A scalable array architecture is used to allow an extension to systems of larger dimensions and other frequency bands. The overall array employs the concept of a folded reflectarray antenna [6, 7] with multilayer, dual-polarisation microstrip antenna elements. By means of the proposed space-fed arrangement using this reflectarray architecture, a complex and lossy RF distribution network can be avoided. SiGe MMICs integrated at the backside of the overall manifold provide amplification, phase shifting and T/R switching. These include BiCMOS for digital or mixed signal circuitry, silicon germanium transistors for the active analogue circuits, and, in a first version, nMOS transistors for the switching and reconfiguration parts. In a second step, RF-MEMS switches will be integrated to reduce losses. Beam scanning is intended up to 60° from broadside into all directions.

The paper is organised as follows. Section 2 describes the overall array architecture. Sections 3 and 4 discuss antenna elements and active circuits, respectively, and experimental results of the overall array are given in Section 5.

2 Array architecture

A general cross section of the array arrangement is given in Fig. 1, left side, [8]. In the transmit case, the feed antenna in the centre of the array radiates a wave against the polarisation grid such that the wave is reflected (polarisation and grid lines in parallel). The reflected wave then is received by the antenna elements and guided to one port of the active circuits where the signal is amplified; amplitude and phase are adjusted according to the required transmit diagram. Following this, the signal is re-radiated in the orthogonal polarisation via the same antenna elements. According to the change of polarisation, the outgoing wave

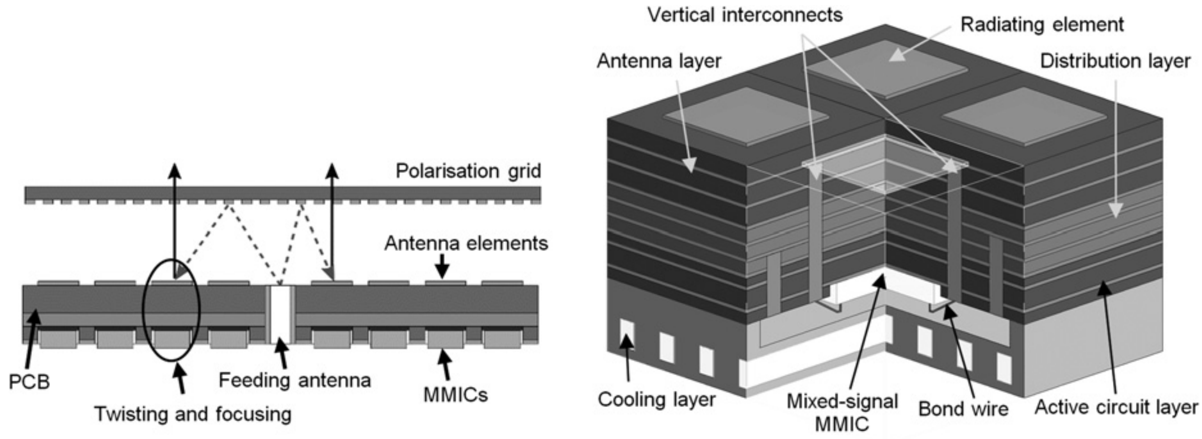

Fig. 1 *Basic cross section of the active folded reflectarray and detailed view on the manifold cross section*

now can pass the polarisation grid. Two example rays are included in the figure.

As a result of the principle of a folded reflectarray, first requirements for the antenna elements are dual-polarisation operation and a good polarisation decoupling between the two antenna ports exceeding the overall gain of the active MMIC. As a matter of course, this decoupling has to be maintained for any array beam position, that is including different couplings between neighbouring elements. According to the required large scanning angle of 60° from broadside, the array also has to be optimised with respect to surface wave resonances and scan blindness at larger angles.

As will be shown in section 3, these properties of the antenna elements are solved based on a multilayer approach with slot and aperture coupling of stacked patches. The necessary multilayer substrate (Fig. 1, right side) includes further (FR4) layers for the distribution of DC and control signals, as well as further microwave substrate layers with interconnects and cavities for the active circuits. Different vertical interconnects provide the required connections between the various layers.

A functional block diagram of the active circuit for a single channel is depicted in Fig. 2. SiGe technology enables the monolithic integration of the different circuit parts, even including MEMS for switching [9, 10]. Details of the functional blocks in this MMIC are given in section 4. Each T/R module consists of a bi-directional vector modulator, two gain blocks (GBs), a low-noise amplifier and a power amplifier. The signal flow direction from polarisation X to polarisation Y, and vice versa is selected using two nMOS single pole, double throw (SPDT) switches. In a further version, the SPDT connected to the polarisation Y antenna port will be replaced by an RF-MEMS component with lower loss. The other SPDT switch, which is less loss sensitive, will remain nMOS to conserve chip area. Two 8-bit digital-to-analogue converters (DACs) set the vector modulator control voltages.

Owing to the small size of the array lattice, it was decided to integrate four channels on one MMIC. An I^2C slave allows serial control of all IC functions, this digital function block is shared by all four T/R modules, which also have the switch control and power-on reset functions in common. A unique bus address for each IC is set by intra-chip wire-bonded jumpers. Combining four T/R modules on one IC results in a larger cell size on the active circuit layer of $10 \times 10\ \text{mm}^2$; in this way, also space is gained for all the necessary bonding pads, vertical interconnects and a metal grid for heat removal from the MMICs. As the top side of the overall manifold is covered with the antenna elements, no major heat transfer is possible via this side. Heat removal via the array edges is excluded as well. As the array shall be scalable, a thick heat removal layer within the multilayer substrate would be necessary, but in this case, a large number of vertical RF interconnects would be rather difficult to realise through such a thick metal layer. Therefore a modified solution has been developed. The lowest RF substrate is not only fabricated with cavities for the ICs but also with a gridded groove structure. Both the IC cavities and the gridded groves are machined down to the metal ground layer of the RF layer serving as the first heat sink. From there, heat is conducted over a very short distance through a metal grid (wall thickness 0.5 mm, height 2.75 mm, sell size $10 \times 10\ \text{mm}^2$) to an external heat sink which, for large arrays, even may include water cooling (Fig. 2 bottom part).

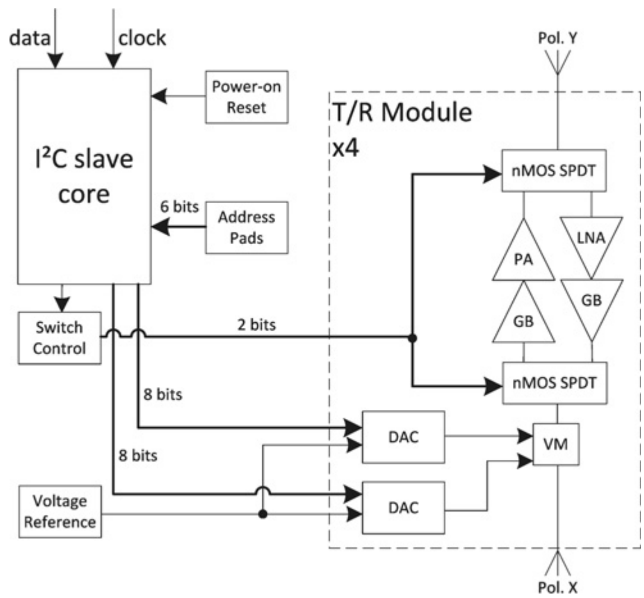

Fig. 2 *Functional block diagram of the active circuit*

PA: power amplifier, LNA: low-noise amplifier, GB: gain block, VM: vector modulator, DAC: digital-to-analogue converter
The two RF ports (Pol. X, Pol. Y) are connected to the two ports (two polarisations) of the antenna element

doi: 10.1049/iet-map.2013.0704

3 Antenna elements

As discussed in the introduction, the antenna elements must fulfil a number of specifications including dual polarisation with very good decoupling and a reasonable operating bandwidth of 29.5 to 30.8 GHz, and all that for a wide angle scanning while avoiding blind angles up to 60°. Preliminary investigations quickly revealed that simple, single layer patch antennas do not meet all specifications, so different multilayer approaches were investigated including slot type elements, slot-patch coupled or stacked patch antennas. Via grids around each antenna cell proved to be an adequate means to reduce the surface wave resonances [11, 12]. Simulation and optimisation of all elements is done with the ANSYS HFSS [13] assuming an infinite array and using periodic boundary conditions. In this way, also the different antenna properties under different scanning angles can be checked. Many approaches exhibit a strong increase in return loss including complete reflection at large scanning angles, especially in the *E*-plane; also coupling between the two polarisations is a critical parameter. Finally, the antenna structure as displayed in Fig. 3, left side, proved to be an optimal one [12].

Antenna cell size, as mentioned before, is chosen to be $5 \times 5\ \text{mm}^2$. The antenna element includes a number of dielectric layers and an air layer with a metal grid structure as support (see Table 1). From the bottom side, a lower square patch is fed via stripline and two orthogonal H-shaped slots. An upper patch, also square, is electromagnetically coupled to the lower one. A 1.65 mm thick air layer, together with a dielectric layer of only 0.127 mm thickness provides a reasonably large bandwidth, a low excitation of surface waves, and a good resistance against scan blindness. As the patch is printed on the lower side of the top substrate, this gives, at the same time, a protective layer for the array. Integrated vertical transitions based on laterally shielded vias finally provide the connections for testing and implementation in a passive array (see section 5). In the active array, extended vertical interconnects provide connections to the layer with the active circuits. A list of all the involved substrate materials is given in Table 1.

Fig. 3, right side, displays the reflection coefficient s_{11} for broadside radiation as well as different scanning angles in the (more critical) *E*-plane. In the operational band, return loss is better than 10 dB even at 60° scanning; it can also be seen that above 32 GHz, the reflection coefficient is close to 0 dB at this angle. For *H*-plane scans, results are considerable better, and no total reflection results. Polarisation decoupling between the two polarisations is better than 27 dB for scanning in both planes.

4 Active circuits

Efforts in the last decade have made SiGe technologies excellent candidates for mm-wave frequency applications based on the high performance of heterojunction bipolar transistors (HBTs). Meanwhile, SiGe HBTs show $f_{\max}$ values of up to 500 GHz [14]. There is a growing interest in providing fully integrated solutions for applications in wideband mm-wave communication or 77 GHz radar [15, 16]. The developments in RF-MEMS technology have also paved the way for achieving high performance and IC-integrated MEMS devices [10, 17, 18]. Among all different types of MEMS integration techniques, the integration of MEMS into a BiCMOS process using an embedded solution appears to be the most promising one for the realisation of fully integrated multi-band and reconfigurable transceivers.

In Fig. 2, the functional block for one active T/R channel was already shown and discussed. This section shall discuss important function blocks.

The low-noise amplifier has a single-stage cascode topology using HBTs. The amplifier has a measured gain of 14 dB at 30 GHz (3 dB higher than simulated), and a simulated noise figure of 3.9 dB. Proper device scaling places the noise equivalent source reflection coefficient towards the centre of the Smith chart. Together with the low equivalent noise resistance of HBTs, this ensures an almost flat noise figure from 20–40 GHz, with only ±0.5 dB variation.

Table 1 Layer structure of the antenna element of Fig. 4

Layer	Material	Thickness, mm	Diel. constant
1	RT Duroid 5880	0.127	2.22
2	Air	1.65	1
3	RT Duroid 5880	0.381	2.22
4	RO 3003	0.127	3
5	RO 3003	0.508	3
6	RO 3003	0.127	3

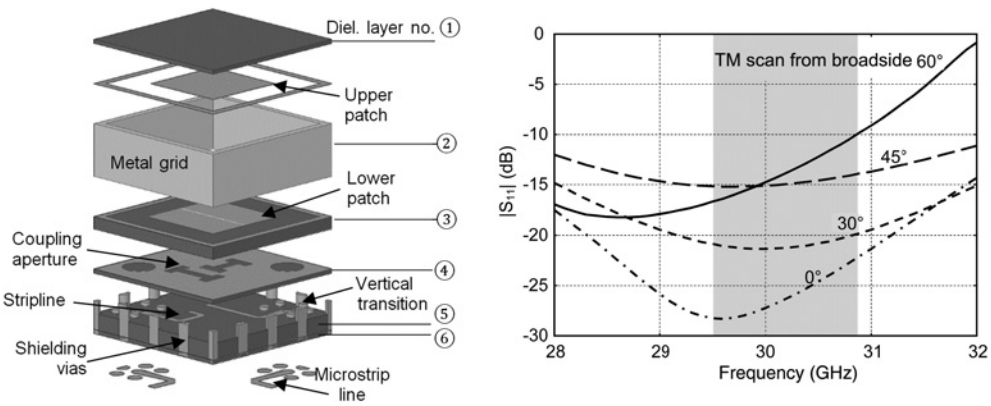

Fig. 3 *Exploded view on the antenna element as used in this array (dielectric layer data are given in Table 1) and simulated reflection coefficient $|S_{11}|$ for various scanning angles in the E-plane of the dual-linear polarised stacked patch antenna*

The frequency range of interest is indicated by grey shadow

doi: 10.1049/iet-map.2013.0704

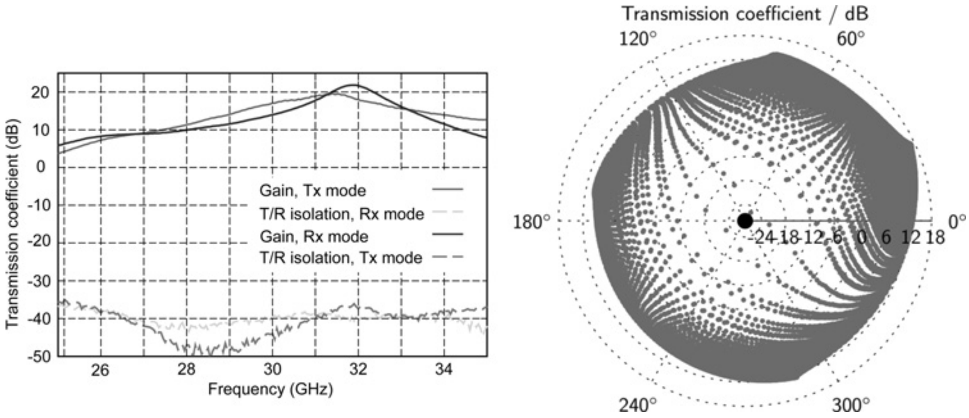

Fig. 4 *Gain and isolation of transmit and receive paths of a T/R module with the vector modulator set for maximum gain and variation of phase and amplitude states in the receive direction at 30 GHz*

The gain is further boosted by a GB, which is identical for the transmit and receive path. Each gain block contains two cascode stages with inductive loads. It provides additional 19 dB of gain at 30 GHz, with an output referred 1 dB compression point of 0 dBm.

The power amplifier has a single-stage, common-base HBT topology with a parallel resonant tank circuit load and reactive input and output matching circuits. It has 8.5 dB gain and an output power of 7 dBm at 1 dB gain compression. The power-added efficiency at gain compression is 8%.

The nMOS SPDT switches have a double-shunt, pi network topology in each arm. The 30 GHz insertion loss is <3.5 dB, the isolation is >30 dB. The switches were designed using a custom switch model and show excellent agreement between simulation and measurement.

The bi-directional vector modulator uses a lumped-element branch line coupler, where the two quadrature ports are loaded by nMOS transistors operated in the linear regime (low V_{DS}). The DAC outputs vary the gate–source voltage of these transistors. A critical issue in these configurations is the non-linearity because of self-biasing effects in the nMOS loads. Here, no gain compression was observed up to 7 dBm input power where the power amplifier starts to saturate.

The IC with only the nMOS switches has been tested in detail in a separate measurement setup. Fig. 4, left side, shows gain and isolation for both the transmit and receive branches of a single T/R module. The measured gain at 30 GHz is 14 dB for the transmit case, and 17 dB in the receive case. Note that the gain maxima have been shifted upwards from the design frequency of 30 GHz. The reason is under investigation. Fig. 4, right side, shows the complex transmission coefficient in a polar representation, demonstrating the gain and phase variation range. Fig. 5 shows a micrograph of the processed four channel IC with nMOS switches. The central part contains the common digital functionality for the four T/R modules. The four identical T/R modules are recognised in pairs on the right and left sides of the IC.

5 Simulated and experimental results of the overall array

5.1 Passive array

Both the antenna elements and active circuits have been tested experimentally in separate setups; in a relatively early state; however, we wanted to have evidence of the performance of an array. To this extent, a number of passive arrays with 108 antenna elements each were designed and fabricated, using already the antennas as intended for the active array. The active circuits are replaced by microstrip lines the lengths of which are adjusted to provide the suitable phase distribution for a number of scan angles, resulting in arrays with fixed beam configurations. These include a broadside beam and scanned beams up to 60° in different planes. A photograph of overall antenna and the reflector substrate of such an array are shown in Fig. 6. The printed polarising grid (RT Duroid 5880, thickness: 3.18 mm, line width: 0.35 mm, centre-to-centre distance of lines: 0.8 mm, metallisation thickness: 17 µm) is placed at a distance of 15 mm in front of the array, held by a Perspex ring.

As examples, 30 GHz radiation diagrams are shown for an array adjusted for broadside radiation and another one for a scan angle of 60° in the more critical *E*-plane (Fig. 7). For

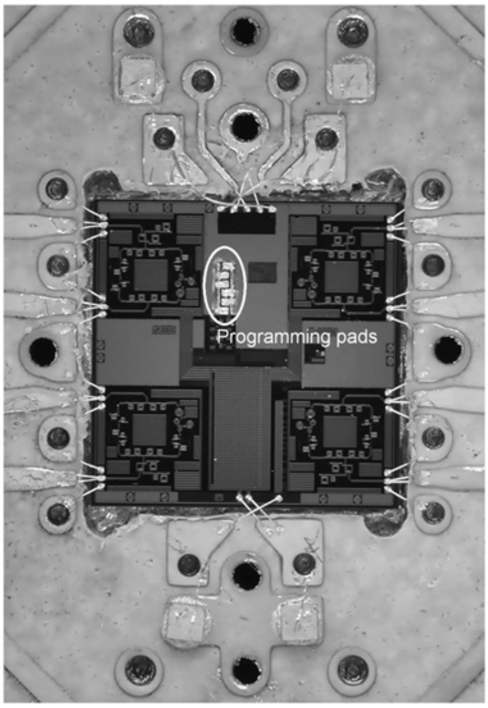

Fig. 5 *Micrograph of the processed four channel IC already integrated into the active array. Chip size is 4 mm × 3.85 mm*

doi: 10.1049/iet-map.2013.0704

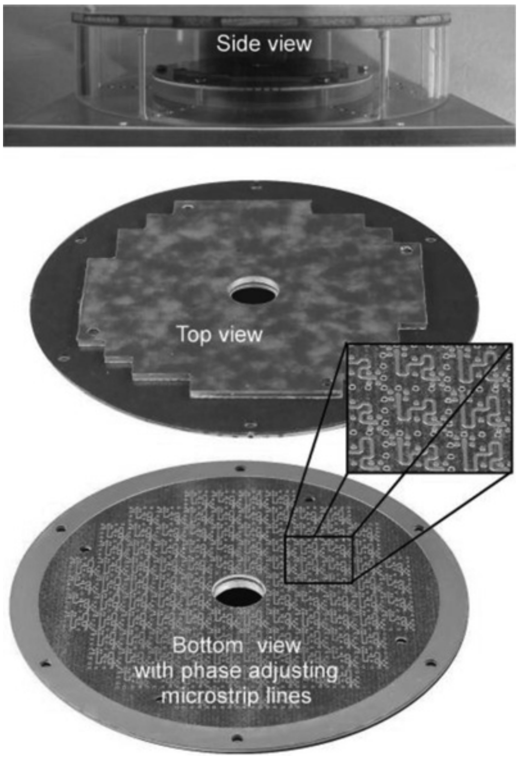

Fig. 6 *Side, top and bottom view of the passive array with microstrip lines to adjust the required phase angles for a fixed beam direction*

the broadside beam array, both simulated and experimental results are plotted. Owing to the large and complex structure, simulations could only be done with limited accuracy; so these can give only a rough comparison. Apparently, experimental sidelobe levels of –19 dB and –17 dB for the *E*- and *H*-plane, respectively, as well as cross polarisation levels of well below 20 dB in both planes are better than the simulated values. For the 60° scanned array, only measurements are available; a full-wave simulation simply is beyond the possibilities of our computers. Maximum of the beam amplitude in the *E*-plane is at 53°, and 60° is covered with only 1.5 dB amplitude reduction. The slight deviation of scan angle probably is because of element coupling not taken into account in the design of the fixed delay lines. Sidelobe level in this plane is about −14 dB. In the orthogonal plane (through the tilted beam), a very clean diagram results with a maximum sidelobe level of about −17 dB. For lower scanning angles, even better results could be stated.

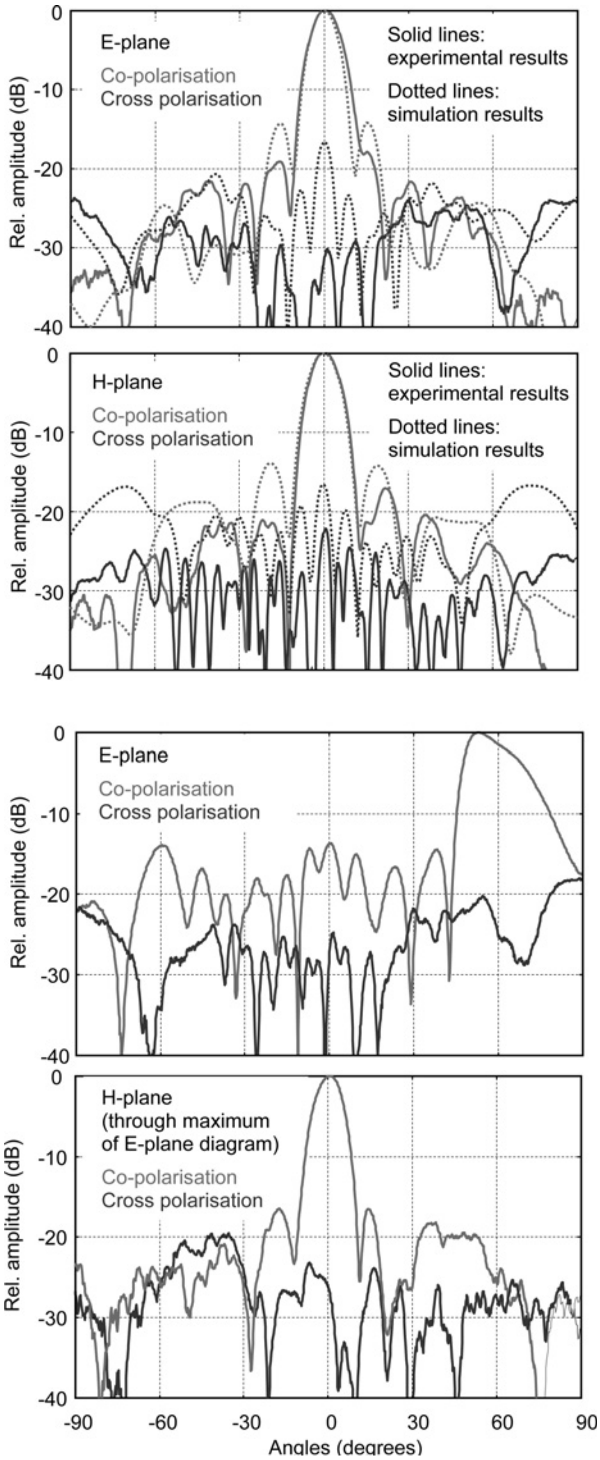

Fig. 7 *E- and H-plane radiation diagrams of a passive test array with fixed broadside beam (top two diagrams) and of a beam designed for 60° scan in the E-plane, the H-plane is measured in a plane through the main beam (bottom two diagrams)*

Red lines: co-polarisation; blue: cross polarisation

5.2 Active array

In a next step, the multilayer substrate has been extended with the layers required for the active circuits. Two different MMICs have been fabricated, one with nMOS switches, one with MEMS switches to take advantage of the low-loss performance of the switches; because of a delayed packaging process of the MEMS switches; however, these MMICs could not be implemented and tested in the array until this paper was finalised. Results on the MMIC with nMOS switches were described earlier in Section 4. After fabrication of the PCB manifold, the MMICs as well as the metal grid for heat removal were glued into the cavities and grooves in the active layer substrate, respectively; interconnects between MMICs and manifold were bonded. Special on-chip bond pads were activated to adjust individual addresses (see Fig. 5). An initial check revealed that 4 of the 36 chips did not function, 32 chips were working properly (see inset in Fig. 8), and accordingly, only 128 out of 144 active antenna elements were available. This array nevertheless was calibrated, and a number of diagrams were recorded. The distribution of defect MMICs

doi: 10.1049/iet-map.2013.0704

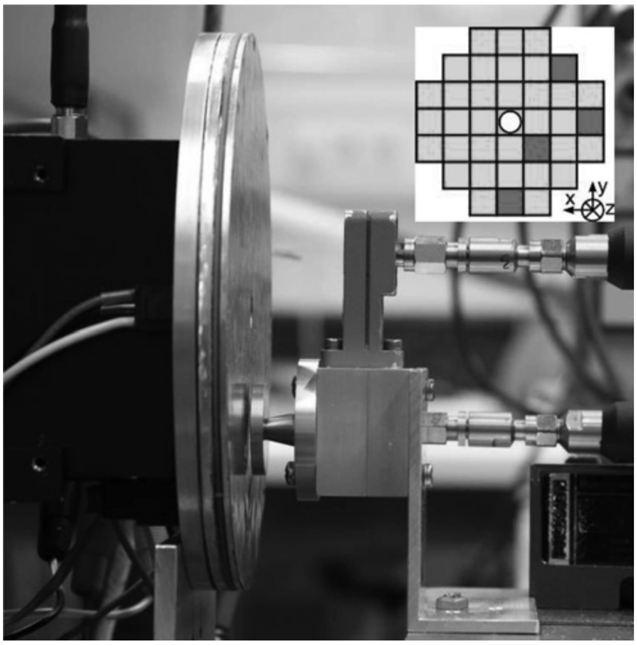

Fig. 8 *Antenna array in the calibration setup and map of working cells (inset picture)*

Light grey: working, dark grey: defect

is not symmetric; therefore, also somewhat unsymmetrical radiation diagrams should be expected.

In operation, the overall array requires a current of 3.3 A and 4.9 A in the RX and TX mode, respectively, at a supply voltage of 2.5 V. A thermal camera recorded temperatures of the array of 33°C and 37°C for the two states with an ambient temperature of 20°C, indicating a sufficient operation of the cooling structure.

5.2.1 Calibration

As the different MMICs with the four TR/TX channels on the chips exhibit fabrication tolerances and non-linear behaviour of the vector modulators with respect to the control voltages, a calibration is necessary before adjusting and measuring radiation diagrams. This calibration is done in the near field of the array (without polarising grid, see Fig. 8). According to the polarisation twisting within this array, an orthomode transducer (OMT) based on [19] was designed and fabricated. It is connected to a small horn including corrugations on the front side to decouple signals to neighbouring antenna elements. A photograph of the antenna array and the probe adjusted for calibration measurements is displayed in Fig. 8. Two ports of a vector network analyser (VNA) in transmission mode are connected to the two ports of the OMT. The array under test is mounted to a near field scanner; the probe (OMT with the horn) is placed on a table in front of the scanner with 1 mm distance between probe and antenna element. In a very first step, the origin of the used coordinate system is determined by scanning for the feed horn in the centre of the array. Following this, the different array elements are automatically and step by step moved in front of the probe. A signal is sent to one port of the OMT; this is fed with one linear polarisation into the array element under test. After processing by the active chip, the signal is returned in the orthogonal polarisation and received by the VNA; in that way, amplitude and phase of the respective array channel can be measured.

To calibrate each channel for both RX and TX mode, a first step is taken to find the two control voltages of the vector modulator for minimum amplitude response based on a simple gradient method. Then control voltage combinations for a relevant number of combinations of amplitude and phase (or respectively, positions in the complex plane of the transmission coefficient) are determined and stored as calibration values. For the array under test here, a dynamic range of 40 dB could be stated. Furthermore, by activating neighbouring elements, an element to element isolation during calibration of better than 30 dB could be stated. Once calibration data for all array elements are available, the respective amplitude and phase values for a given antenna diagram can be determined and the necessary control voltages adjusted using the stored calibration values.

Measurements are made in both RX and TX mode for broadside and scanned beams in *E*- and *H*-plane. A photograph of the active array in the anechoic chamber is depicted in Fig. 9. The feed horn illuminates the reflectarray (via reflection at the polarising grid) with an edge taper of 6 dB. For the adjustment of all array elements, equal amplitude was selected. Phase angle was adjusted for the respective scan angle. As can be seen from Fig. 4, maximum gain depends to some extent on the specific phase angle, so in a first step, module gain was reduced to about 6 dB such that equal amplitudes were available for all elements. According to the calibration in both RX and TX mode, very similar diagrams result in these modes. Therefore only diagrams in the TX mode are plotted in Fig. 10 for scan angles of 0°, 30°, 45° and 60° in *E*- and *H*-plane. The main beam amplitude was normalised with respect to the broadside beam. For the broadside beam, 3 dB beamwidths of 10° and 9.8° in the *E*- and *H*-plane, respectively, result. Owing to the unsymmetrical position of the defect MMICs, a small shift of the beam direction from 0° occurred, and sidelobe level probably is slightly increased and unsymmetrical. In spite of the defect chips, resulting in 16 missing antenna elements, the radiation

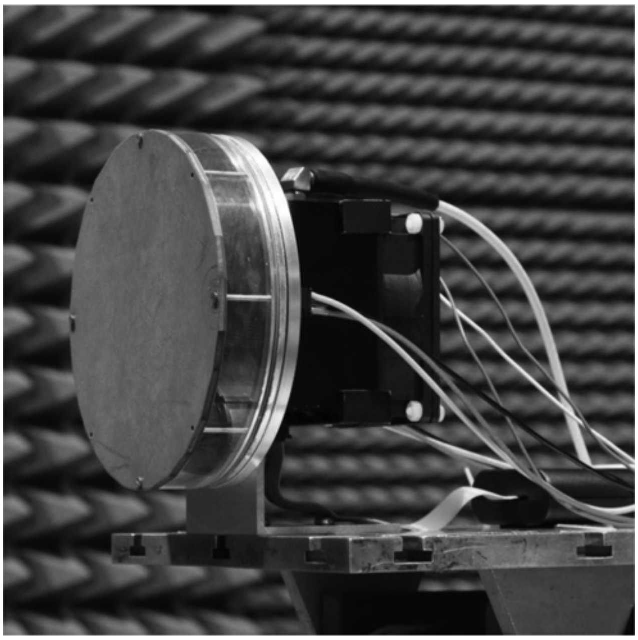

Fig. 9 *Active folded reflectarray mounted in the anechoic chamber*

doi: 10.1049/iet-map.2013.0704

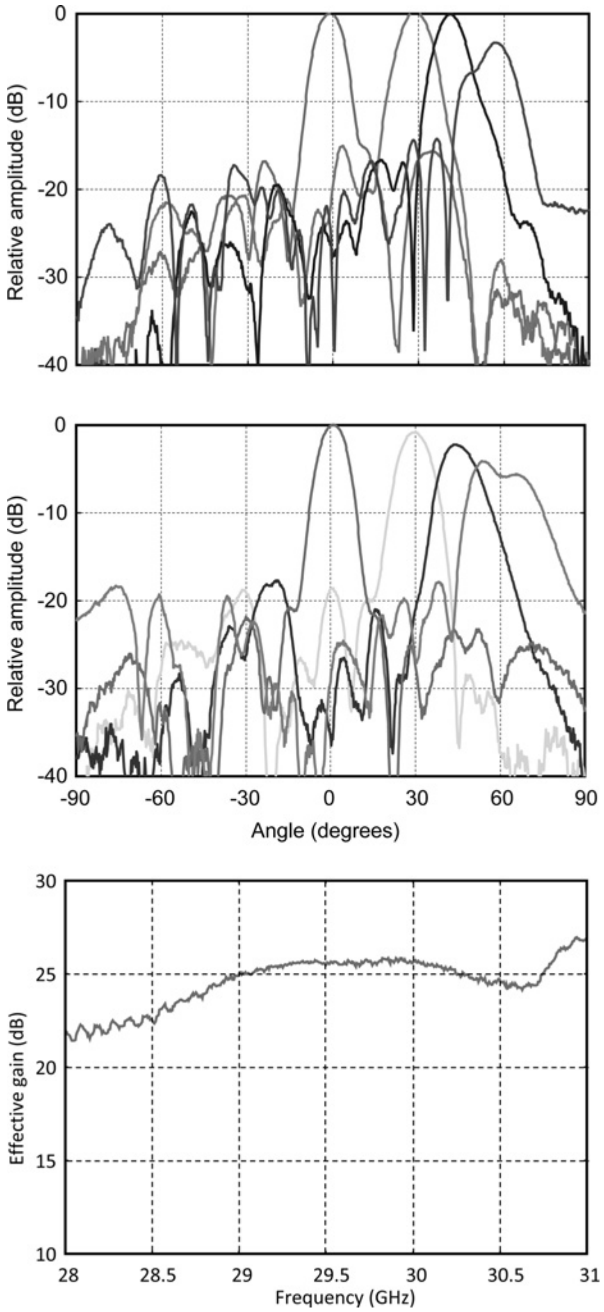

Fig. 10 *Results of the active folded reflectarray*

Top: Radiation diagrams for TX operation; scanning in the *E*-plane with adjusted scan angles of 0°, 30°, 45°, and 60°
Centre: Radiation diagrams of the active folded reflectarray for TX operation; scanning in the H-plane with adjusted scan angles of 0°, 30°, 45° and 60°.
Bottom: effective gain

diagrams show a very good performance, and scanning up to 60° in both planes is demonstrated. As with the passive arrays, the 60° beam does not exactly match the intended angle, but this can be corrected by optimised phase angle adjustments. Simulations also reveal that the missing elements are a main reason for the deteriorated shapes of the 60° beams. In general, the amplitudes of the scanned main beams decrease with increasing scan angle. At 60°, the reductions are 3.3 and 4 dB (with deteriorated beam shape) in the *E*- and *H*-plane, respectively, compared to an expected 3 dB reduction because of the cos(ϑ)-behaviour with ϑ as scan angle. A few tenths of a dB of loss at large scan angles is also because of an increased reflection at the polarising grid. Cross polarisation is determined by antenna elements and polarisation grid; thus, this is very similar to the passive arrays and well below −20 dB (better than −25 dB, except for a residual main beam response, which is caused by a slight rotational mismatch of antenna and illumination horn). An effective gain (antenna gain plus module gain) results in 25.7 dB, resulting for the antenna alone in about 20 dB (including feed-through structures and bonding to the MMICs) or an aperture efficiency of 25% (including the effect of the defect MMICs). Fig. 10, (bottom) shows the gain in this configuration as a function of frequency. Its value is relatively flat within the band of interest, but according to the shift of MMIC amplification to higher frequencies (see Fig. 4), gain increases above 30.7 GHz. Radiation diagrams do not change very much between 29.5 and 31 GHz, except for a slightly increased sidelobe level at 31 GHz.

In a second step, gain of the MMICs was increased by 3 dB where possible. As discussed before, some of the array elements then have a lower gain. Array gain increased by 2.1 dB to 27.8 dB at 30 GHz; the radiation diagrams have similar performance to those depicted in Fig. 10. The overall transmitted power finally depends on the input power and module gain, limited by the maximum output power of the module (in this project, for simplicity only amplifiers with a maximum power of 7 dBm were included).

In a next array with MEMS switches, losses of the switches will be reduced by about 3 dB, resulting in twice the output power in transmit and reduced noise figure in the receive mode. Simulations result in a module noise figure of 8 dB for the nMOS switch version, reduced to 5.3 dB for the MEMS version.

6 Conclusion

A first version of an active scanning array at 30 GHz is presented. The array is based on the principle of a folded reflectarray antenna with multilayer, dual-polarised patch antennas and SiGe MMICs including T/R switches based, in the first approach reported here, on nMOS transistors. In a later version these will be replaced by MEMS switches to reduce losses. The MMICs include four channels each together with a digital circuitry to address and control the different channels.

After tests with passive array prototypes with different fixed beam directions, an active array with 144 antenna elements was fabricated and tested successfully. Although 4 of 36 MMICs did not work, very good radiation diagrams could be measured, and beam scanning up to 60° both in *E*- and *H*-plane could be demonstrated.

Based on this demonstrator, dedicated solutions for different applications in communication and sensing may be realised.

7 Acknowledgment

This work has been funded by the European Union under the project FP7-ICT-2009-5 (FLEXWIN, www.flexwin.eu).

8 References

1 Marcellini, L., Forti, R., Lo Bellaveglia, G.: ‘Future developments trend for Ku and Ka antenna for Satcom on the move’. Proc. 5th European Conf. Antennas and Propagation (EuCAP), April 2011, pp. 2346–2350

2 Feltrin, E., Weller, E.: 'New frontiers for the mobile satellite interactive services'. Advanced Satellite Multimedia Systems Conf., 2010, pp. 155–161

3 Meniconi, E., Sorrentino, R., Chaloun, T., Ziegler, V.: '3D integration technologies for a planar dual band active array in ka-band'. Proc. European Microwave Conf., Nuremburg, Germany, 2013, pp. 215–218

4 Vaccaro, S., Tiezzi, F., Llorens, D., Rua, M.F., De Oro, C.D.G.: 'Ku-Band low profile antennas for mobile satcom'. Proc. 4th Advanced Satellite Mobile Systems (ASMS), 2008, pp. 24–28

5 Stark, A., Dreher, A., Fischer, H., *et al.*: 'SANTANA: Advanced electronically steerable antennas at Ka-band'. Proc. 3rd European Conf. Antennas and Propagation (EuCAP), 2009, pp. 23–27

6 Pilz, D., Menzel, W.: 'Folded reflectarray antenna', *Electron. Lett.*, 1998, **34**, (9), pp. 832–833

7 Menzel, W., Pilz, D., Al-Tikriti, M.: 'MM-wave folded reflector antennas with high gain, low loss, and low profile'. IEEE AP Magazine, June 2002, pp. 24–29

8 Chaloun, T., Meniconi, E., Purtova, T., Ziegler, V.: 'A planar, scalable active transceiver array for mobile Satcom applications'. IEEE Radio and Wireless Symp. (RWS), 2013, pp. 106–108

9 Schumacher, H.: 'Multi-functional Si/SiGe BiCMOS ICs in complex and reconfigurable mm-wave systems'. Proc. ESTEL Conf., Rome, 2012

10 Valenta, V., Kaynak, M., Liu, G., *et al.*: 'From enabling technology to applications: Reconfigurable SiGe BiCMOS ICs with fully integrated RF MEMS switches for millimetre wave transceivers'. Proc 2012 ESA Microwave Technology and Techniques Workshop, Noordwijk, The Netherlands, 21–23 May 2012, pp. 1–8

11 Zhou, D., Zhang, C., Gao, S., Chaloun, T., Menzel, W., Ziegler, V.: 'New multi-layer millimetre-wave folded reflectarray antennas for satellite communications'. Proc. 6th European Conf. Antennas and Propagation (EuCAP), 2012, pp. 821–824

12 Chaloun, T., Menzel, W.: 'Dual-polarized stacked patch antenna for wide scanning reflectarrays up to 60°', *IEEE Trans. Antennas Propag,* submitted

13 Ansys HFSS version 14.0.1, Canonsburg, PA, USA, 2012

14 Heinemann, B., Barth, R., Bolze, D., *et al.*: 'SiGe HBT technology with f_T/f_{max} of 300 GHz/500 GHz and 2.0 ps CML gate delay'. Proc. Electron Devices Meeting (IEDM), 2010, pp. 30.5.1–30.5.4

15 Rebeiz, G.M., Koh, K.-J.: 'Silicon RFICs for phased arrays', *IEEE Microw. Mag.*, 2009, **10**, pp. 96–103

16 Babakhani, A., Guan, X., Komijani, A., Natarajan, A., Hajimiri, A.: 'A 77 GHz phased-array transceiver with on-chip antennas in Silicon: receiver and antennas', *IEEE J. Solid-State Circuits*, 2006, **41**, pp. 2795–2806

17 Fedder, G.K., Howe, R.T., King Liu, T.-J., Quévy, E.P.: 'Technologies for cofabricating MEMS and electronics', *Proc. IEEE*, 2008, **96**, pp. 306–322

18 Kaynak, M., Purdy, M., Wietstruck, M., Zhang, W., Tillack, B.: 'A CMOS based fast high-voltage generation circuit for BiCMOS embedded RF-MEMS applications'. Proc. 13th Topical Meeting on Silicon Monolithic Integrated Circuits in RF Systems (SiRF 2013), pp. 21–23

19 Chang, C., Church Tantaw, S., Voll, P., Sieth, M., Devaraj, K.: 'Theory and experiment of a compact wave-guide dual circular polarizer', *Prog. Electromagn. Res.*, 2012, **131**, pp. 211–225

doi: 10.1049/iet-map.2013.0704